

Contents lists available at ScienceDirect

Nano Energy







High-throughput screening of dual atom catalysts for oxygen reduction and evolution reactions and rechargeable zinc-air battery

Mohsen Tamtaji ^a, Min Gyu Kim ^b, Zhimin Li ^c, Songhua Cai ^c, Jun WANG ^d, Patrick Ryan Galligan ^d, Faan-Fung Hung ^a, Hui Guo ^a, Shuguang Chen ^a, Zhengtang Luo ^{d,*}, Wenting Wu ^{e,*}, William A. Goddard III ^{f,*}, GuanHua Chen ^{a,g,**}

ARTICLE INFO

Keywords: Single atom catalyst Overpotential Electrocatalyst Spin state Machine learning Descriptor

ABSTRACT

We provide the rational design of dual atom catalysts (DACs) supported on nitrogen-doped graphene for the oxygen reduction reaction (ORR) and oxygen evolution reaction (OER) through high-throughput computational screening of M1M2N6-DAC systems, where M1 and M2 represent Fe, Co, Ni, Ru, Rh, Pd, Os, Ir, or Pt metals. We predict that FeRuN6-DAC at the summit of the volcano plot exhibits a low theoretical ORR overpotential (n^{ORR}) of 0.24 V and a low theoretical OER overpotential (η^{OER}) of 0.19 V. The low η^{ORR} and η^{OER} result from the catalytic performance of the Fe site being tuned to electronic properties that facilitate adsorption and desorption of the OH* intermediate. Inspired by these hybrid density functional theory (DFT) computational and machine learning (ML) results, we synthesized FeRuN6-DAC, FeN4-SAC, and RuN4-SAC and characterized them using Xray photoelectron spectroscopy (XPS), X-ray absorption spectroscopy (XAS), scanning transmission electron microscopy (STEM), and in-situ electron spin resonance (ESR). Our in-situ ESR spectroscopy signifies that the spin of the Fe active site increases with increasing applied potential due to the increase in the concentration of OH* intermediate on Fe. We verified experimentally the predicted catalytic performances, finding that FeRuN6-DAC leads to an experimental ORR overpotential of 0.29 V with a Tafel slope of 104 mVdec-1 and an OER overpotential of 0.27 V with a Tafel slope of 124 mVdec⁻¹. The rechargeable Zinc-air battery setup was fabricated with FeRuN6-DAC in place of the cathode, showing a maximum power density of 0.45 W/cm2 at the current density of 0.44 A/cm² and good stability after 120 cycles. According to our findings, we demonstrate that DFTguided strategies are useful for designing advanced DACs applicable to ORR, OER, and Zinc-air battery applications.

1. Introduction

Efficient oxygen reduction reactions (ORR) and oxygen evolution reactions (OER) are required for rechargeable Zinc-air batteries and fuel

cells to ensure rapid reaction kinetics towards appropriate discharge and charge processes [1]. Dual atom catalysts (DACs), in which one metal atom normally acts as the active site and another metal acts as the counterpart site, provide high electrochemical performances [2].

^a Hong Kong Quantum AI Lab Limited, Pak Shek Kok, Hong Kong SAR China

b Beamline Research Division, Pohang Accelerator Laboratory (PAL), Pohang University of Science and Technology, Pohang 37673, Republic of Korea

^c Department of Applied Physics, The Hong Kong Polytechnic University, Hunghom, Kowloon 999077, Hong Kong

d Department of Chemical and Biological Engineering, Guangdong-Hong Kong-Macao Joint Laboratory for Intelligent Micro-Nano Optoelectronic Technology, William Mong Institute of Nano Science and Technology, and Hong Kong Branch of Chinese National Engineering Research Center for Tissue Restoration and Reconstruction, The Hong Kong University of Science and Technology, Clear Water Bay, Kowloon 999077, Hong Kong SAR China

^e State Key Laboratory of Heavy Oil Processing, College of Chemistry and Chemical Engineering, Institute of New Energy, China University of Petroleum (East China), Qingdao 266580, China

f Materials and Process Simulation Center (MSC), MC 139-74, California Institute of Technology, Pasadena, CA 91125, USA

⁸ Department of Chemistry, The University of Hong Kong, Pokfulam Road, Hong Kong SAR China

^{*} Corresponding authors.

^{**} Corresponding author at: Hong Kong Quantum AI Lab Limited, Pak Shek Kok, Hong Kong SAR China *E-mail addresses: mtamtaji@connect.ust.hk (M. Tamtaji), keztluo@ust.hk (Z. Luo), wuwt@upc.edu.cn (W. Wu), wag@caltech.edu (W.A. Goddard III), ghc@everest.hku.hk (G. Chen).

Previous works have reported theoretical calculations and experimental efforts to synthesize and use DACs for the CO2 reduction reaction (CO2RR), hydrogen evolution reaction (HER), nitrogen reduction reaction (NRR), ORR, and OER [3-16]. By using the counterpart metal next to the active metal site in DACs structure, the spin state, d orbital electron distribution, and electronic structure of the metal sites can be regulated by exchanging charges through ligands [17]. For instance, the spin state of Fe sites has been regulated by introducing the Mn counterpart metal, resulting in enhanced ORR performance [18]. Similarly, the non-bonding effect of Ni counterpart sites was reported to modify the electronic properties and spin state of Fe active sites towards enhanced CO2RR and ORR [19,20]. It was also reported that the presence of Zn counterpart sites can modify the d-orbital electron distribution of Cu active sites, enhances the O-O cleavage and promotes the adsorption and desorption of ORR intermediates towards enhanced electrocatalytic activity [21].

Although several studies have been reported on the application of DACs for ORR and OER, a significant challenge in the discovery and development of DACs is how to find the best combination of two metal atoms in the vast parameter space. For example, the use of 9 transition metal atoms in the DAC structure leads to 72 pairwise combinations to be calculated towards enhanced ORR and OER. To solve this problem, we use high-throughput computational screening.

Here, we apply density functional theory (DFT) calculations to predict high-performance M₁M₂N6-DACs, in which M₁ and M₂ represent Fe, Co, Ni, Ru, Rh, Pd, Os, Ir, or Pt metals towards ORR and OER. Accordingly, Fe metal in FeRuN6-DAC was found to have the best ORR and OER overpotentials of 0.24 V and 0.19 V, respectively, better than FeN4-SAC which led to ORR and OER overpotentials of 0.43 V and 0.58 V, respectively, and RuN4-SAC with ORR and OER overpotentials of 1.08 V and 0.83 V, respectively. Therefore, we observed that the interplay of the Ru atom can considerably modulate the ORR and OER activities of the Fe site. Based on these DFT results, we synthesized and characterized FeRuN6-DAC, FeN4-SAC, and RuN4-SAC samples. Then the ORR and OER performances of the synthesized samples were measured, where we found low experimental ORR and OER overpotentials of 0.29 V and 0.27 V, respectively, indicating high ORR and OER performances for FeRuN6-DAC, consistent with our DFT results. The rechargeable Zinc-air battery setup was fabricated with FeRuN6-DAC in place of the cathode, showing good performance and stability after 120 cycles. Our findings suggest that employing the DFT-guided rational design of DACs has the potential to expedite the discovery of enhanced DACs.

2. Materials and methods

2.1. Chemicals

Ultrapure deionized water (DI, 18.2 M Ω) and Graphite with an average particle size of 350 mm (grafguard) are used. KMnO₄, Nafion (5 wt%), H₂SO₄ (95%), KOH (>85%), H₂O₂ (30 wt%), acrylamide (99%), FeCl₃•6H₂O (97%), and RuCl₃•xH₂O (99.9%) are purchased from Sigma Inc. USA. Ethanol (96%) is purchased from the Merck Inc. of Germany. All the chemicals are used as received.

3. Synthesis of graphene oxide (GO)

GO is prepared using the modified hummers method [22]. 30 ml of H_2SO_4 (98%) was added to 1 g of microwave-expanded graphite inside a 500 ml round bottom flask, placed in an ice bath. After 2 hours, 5 g of KMnO₄ is slowly added to the suspension, while the suspension was kept stirring at room temperature for an additional 4 hours until the color changed to pale brownish. Then, 50 ml of deionized (DI) water was added to the suspension while the color became brown. After that, 200 ml of DI water was added to the suspension while stirring for another 2 hours at room temperature. Subsequently, to reduce the residual KMnO₄, H_2O_2 (30 wt%) was added dropwise to the suspension

until the solution's color changed to bright green. Following by stirring for another 2 hours, the solution was then allowed to settle for 1 day. The GO solution is then centrifuged and washed at least 9 times with DI water at 15000 rpm for 30 min and reached 8 mg/ml concentration by adding DI water.

4. Synthesis of catalysts

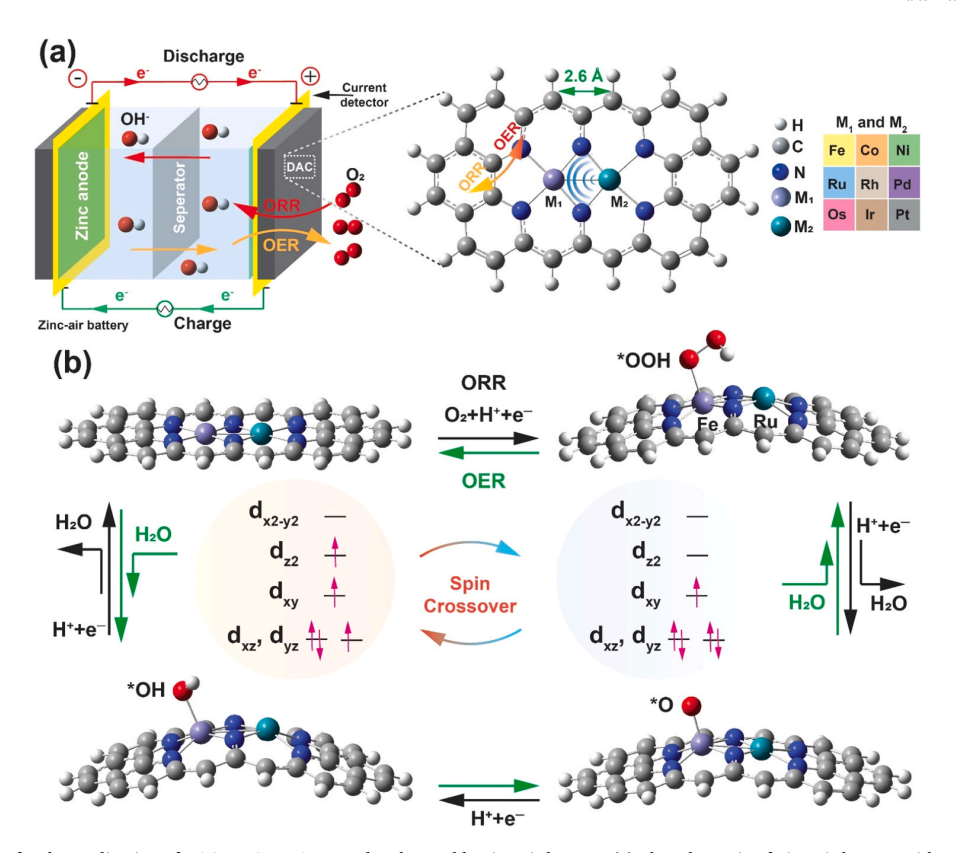
In order to synthesize FeRuN6-DAC, FeCl3•6H2O and RuCl3•xH2O salts as the metal precursors, are used to prepare 0.05 M solutions of Fe^{3+} and Ru^{3+} , respectively [23,24]. 12.5 ml of 8 mg/ml GO was added into 120 ml of DI water containing 125 µl of 0.05 M of Fe³⁺ and Ru³⁺ solutions and 1.2 ml of acrylamides (25 wt%, nitrogen precursor) following by stirring for 36 hours. The suspension is freeze-dried for four days before undergoing a two-step annealing method [25]. The brownish freeze-dried sample (Figure S1a) went through the first annealing step in a 1-inch quartz tube furnace at 450 °C for 3 hours under Ar (200 sccm). Then the blackish sample is washed using H₂SO₄ (0.05 M) and ethanol (96%) five times before being freeze-dried. Subsequently, the freeze-dried sample went through a second annealing process at 590 °C for 3 hours under Ar (200 sccm) to produce blackish FeRuN6-DAC sample (Figure S1b). Similarly, FeN4-SAC and RuN4-SAC as the control samples are prepared with adding only Fe3+ and Ru3+ metal precursors, respectively.

5. Characterization and analysis

The structure and morphology of FeRuN6-DAC, FeN4-SAC, and RuN4-SAC were investigated by scanning transmission electron microscopy (STEM, JEOL JEM-2100 F and aberration corrected STEM, Thermofisher Spectra 300) and scanning electron microscopy (SEM, JEOL JSM-7800 F). Elemental mapping was performed using energy dispersive X-ray analysis (EDX, JEOL JEM 100CXII, and JEOL JSM-7800 F). To determine the metal concentration in the samples, the inductively coupled plasma (ICP) technique was employed using an Optical Emission Spectrometer by Perkin Elmer (Optima 7300 DV). Elemental bonding states were obtained from X-ray photoelectron spectroscopy (XPS) with a PHI 5000 VersaProbe III (ULVAC-PHI). The Fe-K and Ru-K edge X-ray Absorption Fine Structure (XAFS) spectra were acquired through the synchrotron radiation-based Wide-XAFS facility, BL10C at Pohang Accelerator Laboratory (PAL) used to examine the local environment surrounding the Fe and Ru metals. FeRuN6-DAC, FeN4-SAC, and RuN4-SAC samples were then characterized using X-ray diffraction analysis (XRD) (PANalytical) and Raman spectroscopy (Renishaw Raman RM3000 scopes with a 514 nm laser source) to investigate the interlayer spacing, crystallinity, and the ratio of G band to D band. The ORR and OER performances were taken using a rotating ring disk electrode device (RRDE-3A, ALS Co.).

6. Electrocatalytic activity

The ORR and OER experiments were performed by taking 2.5 mg of each of FeN4-SAC, RuN4-SAC, or FeRuN6-DAC samples, 350 μ l of DI water, 150 ml of ethanol, and 50 μ l of Nafion. The suspension was sonicated for 1 day to make a homogeneous black ink. After that, 3 droplets of 10 μ l of ink was dropped on the surface of the neat and clean, glassy carbon electrode (GCE) with a diameter of 0.5 cm and a surface of 0.196 cm². Therefore, the catalyst loading is 0.695 mg/cm². We used a three-electrode cell loaded with 0.1 M KOH aqueous electrolyte for both ORR as well as OER performance measurements. The GCE loaded with catalysts was used as a working electrode, Pt wire was used as a counter electrode, and an Ag/AgCl electrode was used as a reference electrode. The reversible hydrogen electrode (RHE) potentials were then obtained from $E_{RHE}=E_{Ag/AgCl}+0.197+0.0592\times pH$ leading to $E_{RHE}=E_{Ag/AgCl}+0.197+0.0592\times pH$ leading to $E_{RHE}=E_{Ag/AgCl}+0.197+0.0592\times pH$ leading to the 0.1 M KOH electrolyte for 40 min before testing our catalysts. The cyclic



Scheme 1. Schematic for the application of DACs to ORR, OER, and rechargeable Zinc-air battery. (a) The schematic of Zinc-air battery with M_1M_2N6 -DAC. M_1 and M_2 represent Fe, Co, Ni, Ru, Rh, Pd, Os, Ir, or Pt. The metals are anchored on moiety sides. (b) Side view of reaction intermediates along the ORR and OER pathways for FeRuN6-DAC, showing the spin crossover.

voltammetry (CV) tests were conducted with a scan rate of 50 mVs⁻¹ and step size of 5 mV, while the linear sweep voltammetry (LSV) tests were performed from positive to negative potentials with a scan rate of 10 mVs⁻¹, step size of 5 mV, and 2000 rpm rotating speed. To obtain Tafel slopes for ORR and OER, applied potential (vs. RHE) is plotted versus logarithmic scale current density which is obtained from corresponding LSV polarization curves.

In order to conduct Zinc-air battery tests, 59 mg of FeRuN6-DAC, 563 μl of DI water, 563 ml of ethyl alcohol, and 375 μl of Nafion were mixed and the suspension was mixed for 15 minutes to make a homogeneous black ink of the catalyst. Subsequently, the black ink was coated on the carbon cloth with the height of 260 μm and was dried out overnight in an oven with the temperature of 50 °C leading to the loading of 0.97 mg/cm². After that, the carbon cloth coated with the catalyst was utilized as the cathode, a zinc plate with a thickness of 1 mm was used as the anode, and the Zinc-air cell was filled with 6 M KOH electrolyte. Polarization curves were measured at room temperature on a Gamry 5000E workstation to obtain voltage and power density versus current. The galvanostatic discharge-charge curve at 1 mAcm $^{-2}$ under ambient air atmosphere was performed on a Land Battery Test System CT3001A (Wuhan Land Electronic).

7. DFT calculations

Density functional theory (DFT) was carried out in Gaussian 16 software for the geometry optimizations and energy calculations at the Becke, 3-parameter, Lee-Yang-Parr (B3LYP) exchange functional level. The 6–31 G (d, p) basis set was used for C, N, O, and H elements while the LANL2DZ basis set was used for the metals [26,27]. We used the DFT-D3 method to consider van der Waals interactions [28] and the

solvation model density (SMD) to consider solvent (water) effects [29]. In all the DFT calculations, the influence of magnetic coupling was taken into account [15]. Multiwfn 3.8 program was used to obtain electron density and projected density of states (PDOS) [30]. The vibrational frequencies were also calculated to obtain Gibbs free energies.

8. Machine Learning (ML) calculations

Support vector regression (SVR) [31] was applied to predict the Gibbs free energy of reaction intermediates based on DFT-calculated results. NumPy, Scikit-learn, Pickle, and Matplotlib libraries were used in Python 3.7 to read the data, train and save the SVR model, and predict feature importance values. In this work, simple and physically interpretable input features were used to construct an interpretable ML algorithm, [32,33]. Accordingly, the input features used in our SVR model are composed of the intrinsic properties of both the metal atoms (M1 and M2) and also reaction intermediates such as: the atomic radius of metal M₁ (AtR_{M1}), atomic radius of metal M₂ (AtR_{M2}), atomic number of metal M₁ (AtN_{M1}), atomic number of metal M₂ (AtN_{M2}), electronegativity of metal M1 (ENM1), electronegativity of metal M2 (ENM2), ionization energy of metal M1 (IEM1), ionization energy of metal M2 (IEM2), electron affinity of metal M₁ (EA_{M1}), electron affinity of metal M₂ (EA_{M2}), number of d orbital electrons of metal M_1 (θd_{M1}), number of d orbital electrons of metal M_2 (θd_{M2}), and the number of valence electrons of the intermediate (VEint). The input dataset consists of 244 DFT-calculated Gibbs free energies for OH*, O*, and OOH* intermediates and was randomly divided into the training set (90%, 220 data points) and the test set (10%, 24 data points). We used the mean squared error (MSE, equation S12) and R2 value to study the training quality of the SVR model [31]. Subsequently, we used the permutation method [34],

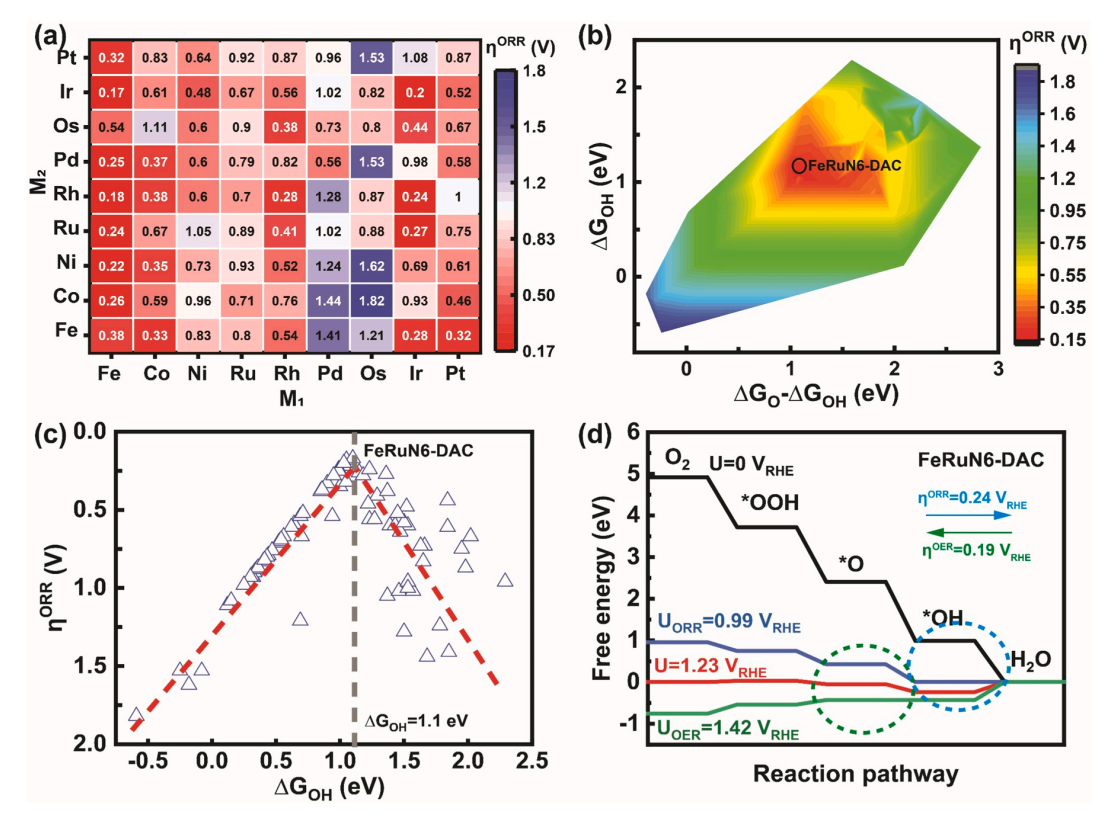


Fig. 1. DFT calculations results. (a) The high-throughput computational screening of ORR overpotential for M_1M_2N6 -DAC, indicating Fe as the most active site with the lowest ORR overpotential. M_1 and M_2 represent Fe, Co, Ni, Ru, Rh, Pd, Os, Ir, or Pt metals. (b) ORR activity volcano plot as a 2D counterplot of overpotentials based on Gibbs free energy of O* and OH* intermediates, indicating that FeRuN6-DAC leads to the low overpotential of 0.24 V_{RHE} . (c) Volcano plot of DFT-predicted η^{ORR} versus ΔG_{OH} , indicating FeRuN6-DAC at the summit . (d) The Gibbs free energy profiles of FeRuN6-DAC with the ORR and OER overpotentials of 0.24 V_{RHE} and 0.19 V_{RHE} .

mutual information (MI) method, and Pearson correlation coefficient [35] to evaluate the influence of each parameter on the model output.

9. Results and discussion

We predicted the Gibbs free energy profiles of M₁M₂N6-DAC (M₁ and M2: Fe, Co, Ni, Ru, Rh, Pd, Os, Ir, or Pt) for ORR and OER and for rechargeable Zinc-air battery. Scheme1a shows a schematic of the rechargeable Zinc-air battery and structure of M1M2N6-DAC using an M₁-M₂ distance of 2.57 Å, based on the DFT-optimized structure. The blue semi-circles signify the influence of M2 metal on the M1 active metal. Here M2 can provide charges to the M1 or take charges from M1 active site through the intervening ligands to tune its spin state and ORR along with OER activities. Scheme1b shows the side views of ORR and OER intermediates, signifying the spin crossover during the reaction [36]. The interplay between the π^* orbital of the reaction intermediates and the d orbitals of the metal active site results in the change in the d-orbital splitting and electron delocalization from low-lying orbitals $(d_{vz} \text{ and } d_{xy})$ to the high-lying orbital (d_{x2-y2}) of M_1 , resulting in the changes in its spin state [36]. OER and ORR may proceed, respectively, through the forward and backward directions of following fundamental steps [37]:

$$* + H2O \rightleftharpoons OH^* + H^+ + e \tag{1}$$

$$OH^* \rightleftharpoons O^* + H^+ + e \tag{2}$$

$$O^* + H_2O \rightleftharpoons OOH^* + H^+ + e$$
 (3)

$$OOH^* \rightleftharpoons O_2 + H^+ + e\overline{+}*$$
 (4)

Due to the difficulties in calculating accurate free energies of OH, O, and OOH radicals in the electrolyte solution, the Gibbs free energies of OH*, O*, and OOH* intermediates are calculated with reference to the free energy of stoichiometrically balanced amounts of H₂O (g) and H₂ (g) [37]:

$$\Delta G_{OH^*} = E_{DAC-OH^*} - E_{DAC} + 0.5E_{H_2} - E_{H_2O} + \Delta ZPE - T\Delta S$$
 (5)

$$\Delta G_{O^*} = E_{DAC-O^*} - E_{DAC} + E_{H_2} - E_{H_2O} + \Delta ZPE - T\Delta S$$
 (6)

$$\Delta G_{OOH^*} = E_{DAC-OOH^*} - E_{DAC} + 1.5E_{H_2} - 2E_{H_2O} + \Delta ZPE - T\Delta S$$
 (7)

 E_{H2} , E_{H2O} , E_{DAC} , E_{DAC-OH^*} , E_{DAC-O^*} , and $E_{DAC-OOH^*}$ are the total energy of H_2 (g), H_2O (g), DAC surface, DAC-OH*, DAC-O*, and DAC-OOH*, respectively. Δ ZPE is the zero-point energy (ZPE) correction at 298 K to consider the enthalpy change from 0 to 298 K. T Δ S is the entropy correction and T is the absolute temperature (298 K).

It is assumed that the Gibbs free energies of the OH*, O*, and OOH* intermediates decrease linearly with the applied potential, regardless of the pH of the electrolyte. [38]. The theoretical ORR and OER overpotentials (η^{ORR} and η^{OER}) can be calculated based on the difference between limiting potential and U=1.23 V_{RHE} as the equilibrium potential. The ORR and OER limiting potentials are the highest potentials at which all the reaction steps are downhill and uphill in free energy, respectively, (see Supporting Information) [39].

Fig. 1a and S14a demonstrate the high-throughput computational screening of ORR and OER overpotentials for M_1M_2N6 -DAC, indicating Fe to be the most active site with low ORR and OER overpotentials, in

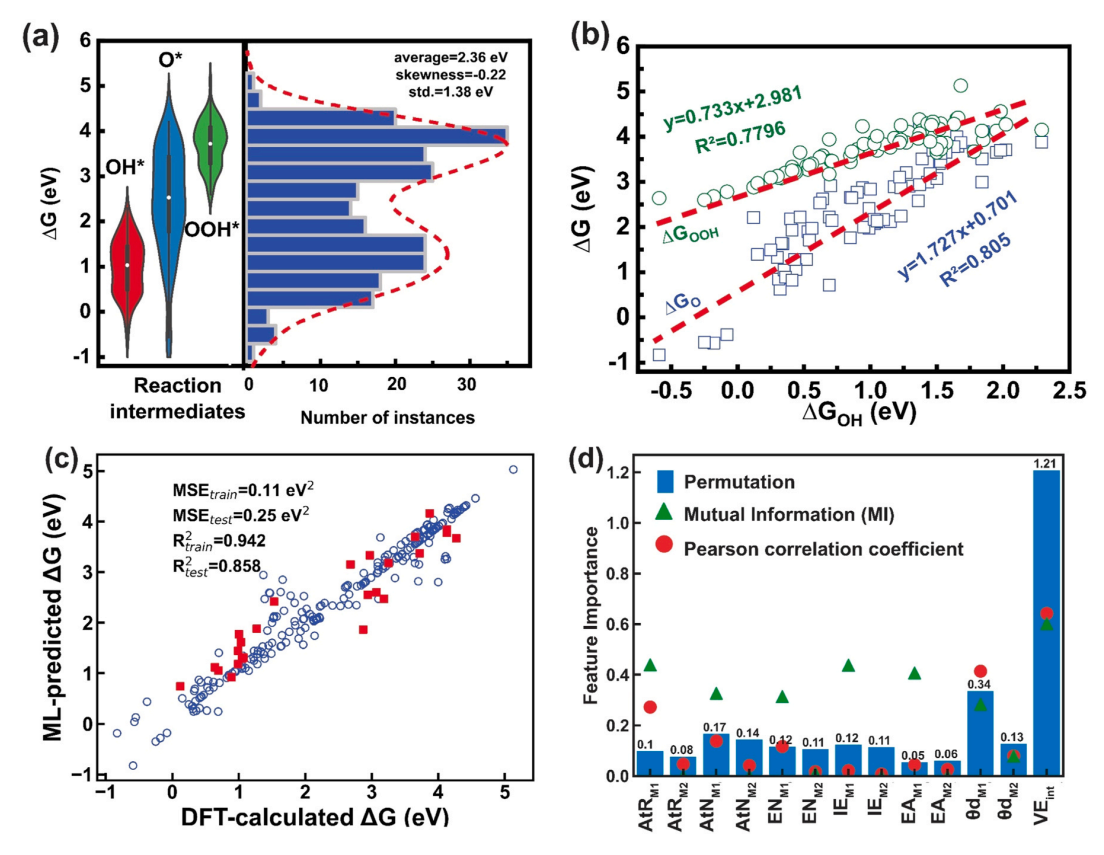


Fig. 2. Machine learning (ML). (a) Violin plot and the histogram of variation of Gibbs free energies obtained from DFT-D3 calculations, containing 244 data points with an average of 2.36 eV and a standard deviation (std.) of 1.38 eV. (b) Weakened scaling relationship limit between OH*, O*, and OOH* intermediates. (c) ML-versus DFT-predicted Gibbs free energies, indicating the good performance of the ML model. (d) Permutation feature importance values along with Mutual Information (MI) and Pearson coefficients. This signifies that the number of valence electrons of the intermediate (VE_{int}) and the number of d orbital electrons of the active metal (θd_{M1}) as the most important parameters.

agreement with previous studies [38]. For example, the ORR theoretical overpotentials for FeCoN6-DAC, FeNiN6-DAC, FeRuN6-DAC, FeRhN6--DAC, FePdN6-DAC, and FeIrN6-DAC are 0.26, 0.22, 0.24, 0.18, 0.25, and 0.17 $V_{\text{RHE}},$ respectively, comparable with DFT-predicted η^{ORR} of 0.43 V for FeN4-SAC [40], 0.28 V for FeCoN6-DAC [40], 0.43 V for the benchmark Pt (111) [37], 0.33 V for CoRu@N8V4 [41], and 0.34 for CoCuN6-gra(OH) [15]. In addition, we predict the OER overpotentials of FeNiN6-DAC, FeCoN6-DAC, FeRuN6-DAC, FeRhN6-DAC, FePdN6-DAC, and FeIrN6-DAC are 0.41, 0.61, 0.19, 0.35, 0.60, and 0.44 V_{RHE} respectively. Therefore, FeRuN6-DAC is predicted to possess the best overpotentials, applicable for both ORR and OER of the rechargeable Zinc-air battery. Fig. 1b and S14b demonstrate ORR and OER activity volcano plots as a 2D counterplot of overpotentials based on the Gibbs free energy of O* and OH* intermediates. They suggest that the ORR and OER overpotentials reach their lowest values around ΔG_{OH} =1.1 eV. Fig. 1c and S14c show the volcano plots of ORR and OER overpotential versus the Gibbs free energy of OH* intermediate, indicating FeRuN6-DAC at the summits. This further indicates that ΔG_{OH} can be used as the descriptor for both ORR and OER activity of dual atom catalysts.

Figure S14d displays OER overpotential (η^{OER}) versus ORR overpotential (η^{ORR}) for $M_1M_2N6\text{-DAC}$. Fig. 1d shows the ORR and OER pathways for FeRuN6-DAC with the ORR and OER overpotentials of 0.24 V_{RHE} and 0.19 V_{RHE} , respectively (see Figure S10 for ORR and OER pathways of FeN4-SAC and RuN4-DAC). Fig. 1d signifies that the ORR potential determining step is the proton transfer to OH*, because this particular reaction step, represented by a blue dashed circle, exhibits a

flat free energy profile at the ORR limiting potential of 0.99 $V_{RHE}.$ Similarly, the OER potential determining step is the deprotonation of OH*, because this reaction step, represented as a green dashed circle, exhibits a flat free energy profile at the OER limiting potential of 1.42 $V_{RHE}.$ From Fig. 1d, the ORR and OER overpotentials of FeRuN6-DAC are $|1.23\text{--}0.99|\text{=-}0.24~V_{RHE}$ and $|1.23\text{--}1.42|\text{=-}0.19~V_{RHE}$, respectively.

We further analyzed the DFT-calculated data for the implementation of machine learning (ML). Fig. 2a shows the violin plot and the histogram of the Gibbs free energies (\Delta G) of OH*, O*, OOH* intermediates obtained from DFT-D3 calculations, including 81 data points for each intermediate and an average of 2.36 eV (the standard deviation (std.) is 1.38 eV and the skewness is -0.22). Fig. 2b indicates a weakened scaling relationship limit between OH*, O*, and OOH* intermediates. This enables us to separately tune the adsorption energy of a specific intermediate toward the desirable electrochemical reaction. Fig. 2c demonstrates ML- versus DFT-predicted Gibbs free energies, indicating a good performance of the ML model with the R2 values of 0.942 and 0.858 and MSE values of 0.11 eV² and 0.25 eV², respectively, for training and test data. Fig. 2d indicates the feature importance values based on the permutation method along with the corresponding Mutual Information (MI, solid green triangle), and Pearson correlation coefficients (solid red circle). This suggests that the number of valence electrons of the intermediate (VEint) and the number of d electrons of the active metal (θd_{M1}) are the most important parameters, in agreement with previous works [32]. This also agrees with volcano plots shown in Fig. 1c and S14c, which suggest that the ORR and OER overpotentials

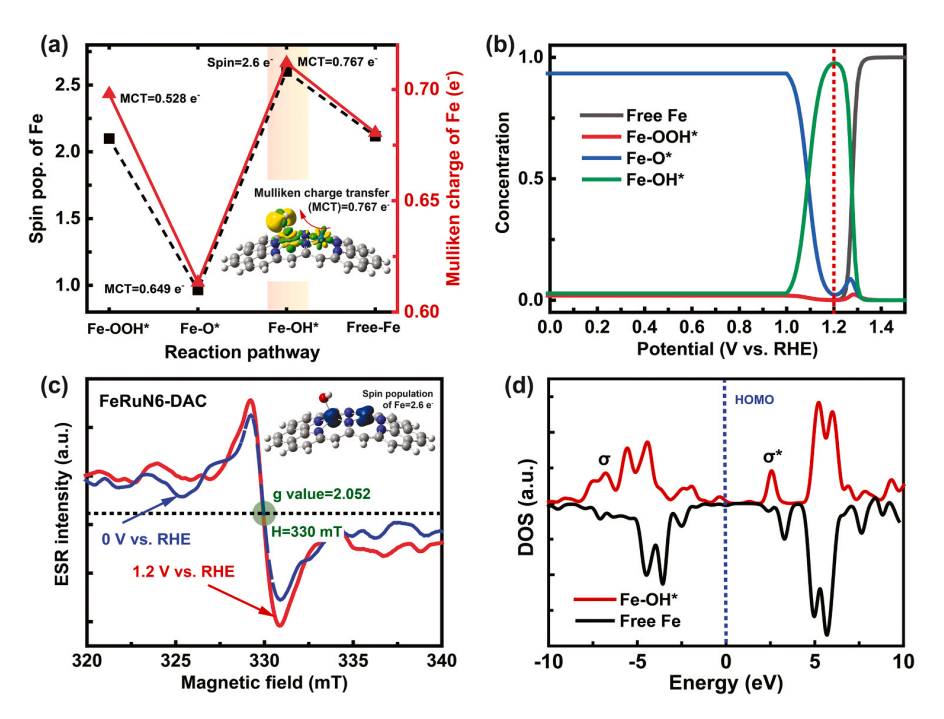


Fig. 3. Spin population and Mulliken charge analysis. (a) The spin population and Mulliken charge of the Fe atom in FeRuN6-DAC along the ORR pathway. This indicates the highest spin values occur after bonding with OH* intermediate. The inset shows the side view of the Mulliken charge transfer to OH* intermediate from FeRuN6-DAC (Isosurface value = 0.01 e/Å^3). Green and yellow colours represent, respectively, the charge deficiency and charge availability. (b) The theoretically-obtained concentration of ORR intermediates on the Fe site of FeRuN6-DAC versus applied potential signifying that at high potentials, the surface is predominantly covered with OH* intermediates. (c) *In-situ* electron spin resonance (ESR) spectra of FeRuN6-DAC obtained at room temperature. This indicates a higher spin population at 1.2 V_{RHE} compared to 0 V_{RHE} . The inset shows the spatial spin density of FeRuN6-DAC bonded with OH* (Isosurface value = 0.005 e/Å^3). Green and blue colours represent the down-spin (beta) and up-spin (alpha) density, respectively. (d) Density of states (DOS) of 3d hybrid orbitals of Fe atom in FeRuN6-DAC before and after the adsorption of OH*.

can be described based on the Gibbs free energy of OH^{\star} intermediate.

We also analyzed the spin state, Mulliken charge, and charge transfer of active sites. Fig. 3a shows the spin population of Fe, Mulliken charge of Fe, and charge transfer from Fe to reaction intermediates in FeRuN6-DAC along the reaction pathway indicating the highest values after bonding with OH* intermediate. The inset shows the side view of Mulliken charge transfer (0.767 e⁻) to OH* intermediate with the Isosurface value of 0.01 e/Å³, in agreement with previous work [40]. Green and yellow colours represent, respectively, the charge deficiency and charge availability. By assuming that the Gibbs free energy of intermediates decreases linearly with the increase in the potential, we may use the Eyring rate equation to roughly calculate the concentration of intermediates along the ORR pathway (see Supporting Information). Fig. 3b depicts the concentrations of O*, OH*, and OOH* intermediates on the Fe site of FeRuN6-DAC verses applied potentials, suggesting that at high potentials, the Fe surface is predominantly covered with OH* intermediate [42]. The proton transfers to OH* and O* intermediates are the rate-limiting steps at high and low potentials, respectively, consistent with previous studies [42]. Subsequently, based on Fig. 3a-b, we conclude that at potentials >1 V_{RHE}, the spin population of the Fe site increases, while at lower potentials the spin population decreases. These findings are consistent with the in-situ electron spin resonance (ESR) spectroscopy results for FeRuN6-DAC. Fig. 3c demonstrates the in-situ ESR spectra of Fe metal measured at room temperature with 1 M KOH electrolyte saturated with O2. This indicates a higher spin population at $1.2\ V_{RHE}$ compared to $0\ V_{RHE}$, which agrees with the theoretical results. In fact, the higher spin population at 1.2 $\ensuremath{V_{\text{RHE}}}$ is due to the saturation of Fe active sites with OH* intermediates. The g-value of approximately 2.052 in the in-situ ESR spectra is attributed to the presence of unpaired electrons in the $3d_{x2-y2}$ and $3d_{z2}$ orbitals of Fe site [43]. The inset shows

the spatial spin density of FeRuN6-DAC bonded with OH* with the Isosurface value of 0.005 e/ų. Green and blue colours represent the down-spin (beta) and up-spin (alpha) density, respectively.

To shed more light on the binding of OH* intermediates with the Fe active site, we provided the density of states (DOS). Fig. 3d depicts the DOS of 3d orbitals at the Fe active site in FeRuN6-DAC before and after the adsorption of OH*. Peaks corresponding to $3d_{z2}$ orbital of Fe atom disappeared and new peaks appeared after the adsorption of OH* which are shown as bonding (σ) and antibonding (σ^*) orbitals [23].

Inspired by the above findings, we synthesized FeN4-SAC, RuN4-SAC, and FeRuN6-DAC samples. The metal loading of the synthesized catalysts was investigated using inductively coupled plasma (ICP), showing:

- the Fe and Ru metal contents are 0.25 and 0.49 wt%, respectively, in the FeN4-SAC and RuN4-SAC samples
- the Fe and Ru metal contents are, respectively, 0.26 and 0.51 wt% in the FeRuN6-DAC sample.

This indicates a molar ratio of almost 1:1 for Fe/Ru. The chemical states of the synthesized catalysts were investigated using X-ray photoelectron spectroscopy (XPS). The N 1 s peak is deconvoluted, to identify different types of nitrogen in the DACs for synthesized samples (Figs. S2–4). For example, Figure S4b displayes that the deconvoluted N 1 s peak for FeRuN6-DAC is composed of pyridinic-N (397.9 eV), Fe/RuN (398.6 eV), and pyrrolic-N (400.0 eV)[23]. Fig. 4a-b displayes a high-resolution XPS peak spectrum for Fe $2p_{3/2}$ and Ru $2p_{3/2}$ of FeN4-SAC, RuN4-SAC, and FeRuN6-DAC, signifying the partially oxidative states [19,38]. The binding energy of Fe $2p_{3/2}$ in FeRuN6-DAC shifts by +1 eV compared with that in FeN4-SAC, indicating a higher

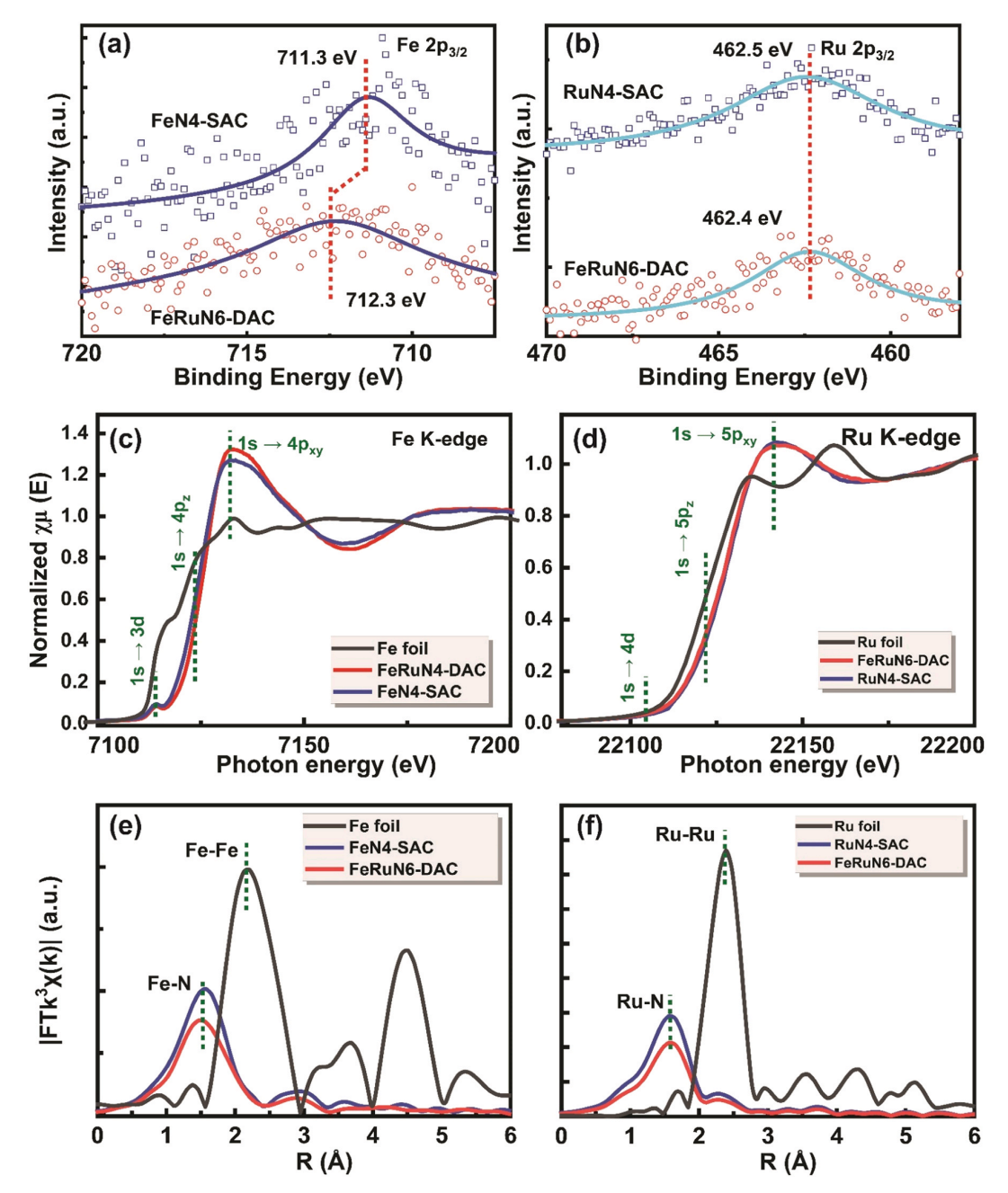


Fig. 4. XPS and XAS characterizations. (a) The high-resolution XPS spectra for (a) Fe $2p_{3/2}$ and (b) Ru $2p_{3/2}$. (c) Fe K-edge and (d) Ru K-edge XANES spectra of our synthesized FeN4-SAC, RuN4-SAC, and FeRuN6-DAC and their corresponding reference bulk samples. Three peaks result from $1 \text{ s} \rightarrow 3d/4d$, $1 \text{ s} \rightarrow 4p_z/5p_z$, and $1 \text{ s} \rightarrow 4p_x/5p_{xy}$ transitions [43]. Fourier transformations (FT) EXAFS spectra in R space of (e) Fe and (f) Ru with their corresponding reference bulk samples. The main peaks attributed to Fe-N and Ru-N are different from Fe-Fe and Ru-Ru peaks, respectively.

oxidation state for Fe in FeRuN6-DAC [19]. This is consistent with the Mulliken charge analysis of Fe, decreasing from $+0.681~e^-$ for FeRuN6-DAC to +0.591 for FeN4-SAC, implying that the Ru site removes electrons from Fe site [44] due to its higher electronegativity (2.2) than Fe (1.83).

XANES and EXAFS were used to study the atomic configuration and electronic states of the Fe and Ru metals in FeN4-SAC, RuN4-SAC, and FeRuN6-DAC samples. Fig. 4c-d depict the Fe and Ru K-edge XANES spectra for, FeN4-SAC, RuN4-SAC, and FeRuN6-DAC, suggesting that the local atomic structure around Fe and Ru metals differs from their Fe

and Ru bulk metals. In Fig. 4c-d, a blue-shift is observed in the Fe and Ru absorption edge when compared to their respective bulk samples, indicating a higher oxidation state than 0 for both Fe and Ru atoms. The observed higher oxidation state is attributed to the coordination environment around the Fe and Ru metals. This coordination leads to a modified electronic structure, which results in the observed blue-shift in the Fe and Ru absorption edges compared to their bulk counterparts [23, 24,43]. In addition, three peaks observed for Fe metal in Fig. 4c are because of $1 \text{ s} \rightarrow 3d$, $1 \text{ s} \rightarrow 4p_z$, and $1 \text{ s} \rightarrow 4p_{xy}$ transitions [43], while three peaks observed for Ru metal in Fig. 4d are because of $1 \text{ s} \rightarrow 4d$, $1 \text{ s} \rightarrow 5p_z$,

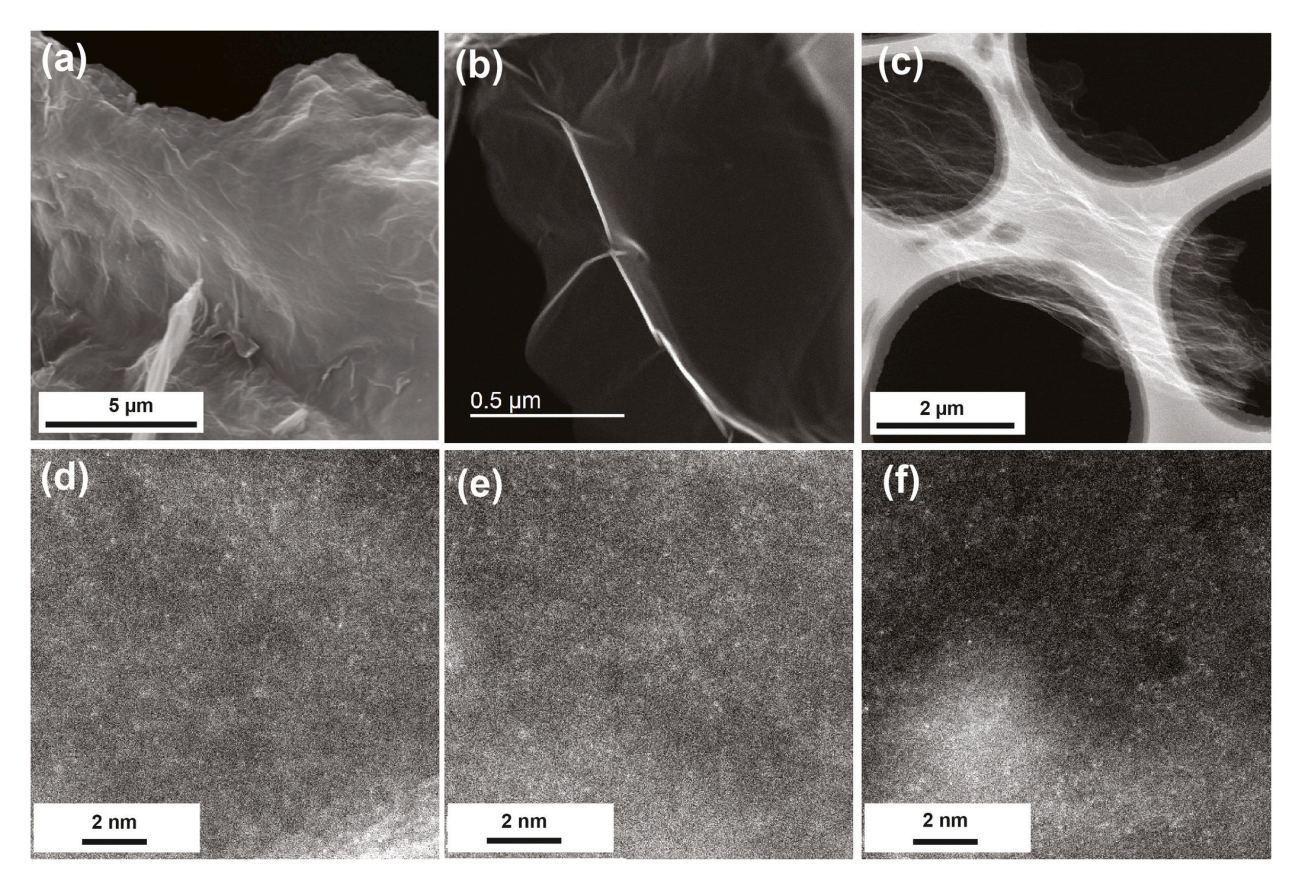


Fig. 5. SEM, TEM, and STEM characterizations. (a) SEM and (b,c) STEM images of FeRuN6-DAC. STEM image of the (d) FeN4-SAC (e) RuN4-SAC, and (f) FeRuN6-DAC samples signifying a homogeneous dispersion of individual Fe and Ru metals (represented as white dots) on the nitrogen-doped graphene support.

and $1 \text{ s} \rightarrow 5p_{xy}$ transitions. The existence of tetravacancy and divacancy-based M₁M₂-N6C6 and M-N4C4 moieties bonded axially with broken D4h symmetry confirms the higher main peak intensity $(1 \text{ s} \rightarrow 4p_{xy}/5p_{xy})$ observed in Fig. 4c-d for Fe and Ru K-edge spectra compared to their respective bulk metals [23]. Moreover, as shown in Figs. 4c, 1s→4pz transition peak in the Fe K-edge XANES spectra of FeRuN6-DAC possesses a blue-shift compared to FeN4-SAC, suggesting a higher oxidation state for Fe in FeRuN6-DAC [44], consistent with our XPS results. The theoretical calculation using the accurate finite difference (FD) approach implemented in the FDMNES software [23,45], can reproduce the blue-shift observed in the Fe K-edge XANES spectra, as shown in Figure S11. It is worth mentioning that the observed changes in both experimental and theoretical XANES spectra of Fe metal are much greater than for Ru metal. This may be attributed to the higher exchange sensitivities in 3d transition metals compared to 4d transition metals [46].

The bonding and coordination environment around the Fe and Ru metals were further confirmed using EXAFS Fourier transform (FT). Fig. 4e-f indicates that the EXAFS FT spectra of FeN4-SAC, RuN4-SAC, and FeRuN6-DAC possess prominent peak associated with Fe-N and Ru-N bonding at around 1.50 Å, distinct from the Fe-O peak observed at 1.55 Å [38] and Fe-Fe and Ru-Ru peaks observed at 2.16 and 4.46 Å. These findings confirm that the coordination environment surrounding the Fe and Ru metals is associated with Fe/Ru-N interactions. Minor peaks, belonging to metal-metal coordination, appear in the EXAFS spectra of RuN4-SAC and FeRuN6-DAC in Fig. 4f, which can be attributed to the noise or the interaction of metal-metal coordination (Fe-Ru) in our catalyst.

The surface morphology, surface structure, and elemental mapping

of FeRuN6-DAC are further investigated by SEM, STEM, and EDX. Fig. 5a demonstrates the SEM imaging of FeRuN6-DAC and Figure S6 shows the EDX elemental mapping, suggesting the uniform presence of Fe, Ru, N, and C elements throughout the nitrogen-doped graphene support. In Fig. 5b,c, the STEM images for the FeRuN6-DAC sample are presented and no significant aggregation is observed. These results are in agreement with the XRD spectrum presented in Figure S5 for FeN4-SAC, RuN4-SAC, and FeRuN6-DAC. The XRD spectra exhibit a single broad graphitic carbon peak at 24.9° (002) corresponding to the interlayer spacing of d=3.6 Å. No additional peaks corresponding to Fe and Ru metals aggregation or their oxides, carbides, or nitrides compounds are detected in the XRD spectra [23]. Fig. 5d-f show the STEM high angle annular dark field (STEM-HAADF) images of FeN4-SAC, RuN4-SAC, and FeRuN6-DAC where the Fe and Ru metals (white dots) are distributed uniformly throughout the entire nitrogen-doped graphene support.

According to the Raman spectra provided in **Figure S7**, the intensity ratio of D band to G-band (I_D/I_G) for FN4-SAC, RuN4-SAC, and FeRuN6-DAC is 0.78, 0.73, and 0.89 leading to a density of defect vacancies (n_D) of 0.0024 nm $^{-2}$, 0.0022 nm $^{-2}$, and 0.0027 nm $^{-2}$, respectively. The rise in the defect density for FeRuN6-DAC is due to the higher metallic species compared to FeN4-SAC and RuN4-SAC [47].

The ORR and OER performances of all synthesized materials in 0.1 M KOH electrolyte were checked using the rotating disk electrode. Cyclic voltammetry (CV) measurements were performed under O_2 - and Arsaturated electrolytes, as provided in **Figure S9**. The CV curve of FeRuN6-DAC under O_2 -saturated electrolyte exhibited a main ORR peak at 0.73 $V_{\rm RHE}$, indicating that dioxygen is reduced by FeRuN6-DAC. Fig. 6a shows the ORR linear sweep volumetry (LSV) of FeN4-SAC, RuN4-DAC, and FeRuN6-DAC samples for the rotation speed of

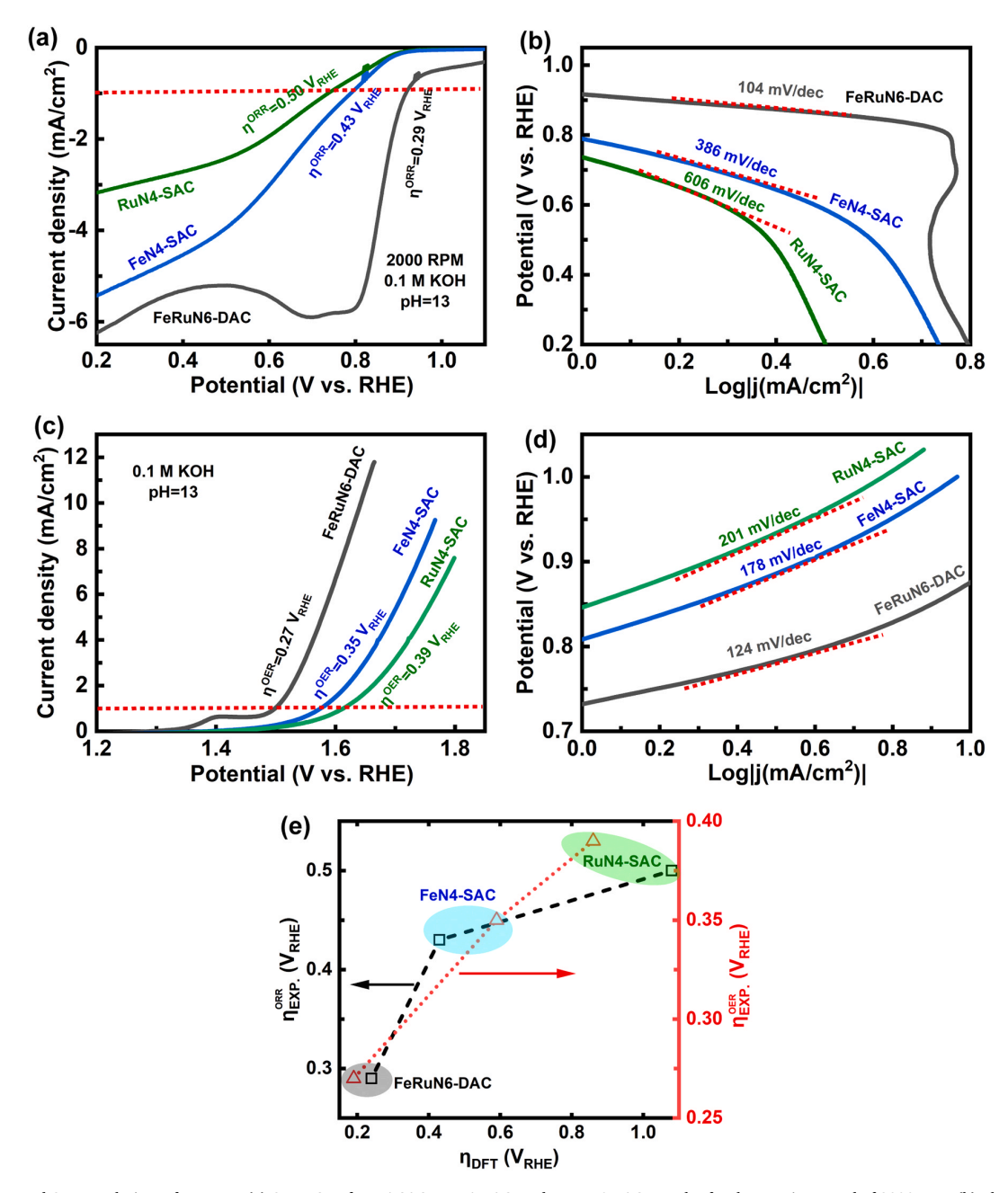


Fig. 6. ORR and OER catalytic performance. (a) ORR LSV of FeN4-SAC, RuN4-DAC, and FeRuN6-DAC samples for the rotation speed of 2000 rpm. (b) The ORR Tafel plot of samples indicates the low Tafel slope of 104 mV/dec for FeRuN6-DAC. (c) OER LSV of FeN4-SAC, RuN4-DAC, and FeRuN6-DAC samples. (d) The OER Tafel plot for various samples indicates the low Tafel slope of 124 mV/dec for FeRuN6-DAC. The catalytic performance of all samples was evaluated in an O₂-saturated electrolyte of 0.1 M KOH. (e) Experimental versus DFT-predicted ORR and OER overpotentials at the current density of 1 mA/cm², indicating good agreement between DFT and experimental results.

2000 rpm under O₂-saturated electrolyte. As provided in Fig. 6a, the ORR onset potential and overpotential for the FeRuN6-DAC sample are +0.94 V_{RHE}, 0.29 V, respectively. The experimental ORR overpotential of 0.29 V is in consistent with the DFT-predicted overpotential of 0.24 V, Fig. 1b. FeN4-SAC and RuN4-SAC display a more negative ORR onset potential compared to FeRuN6-DAC, leading to the ORR overpotentials of 0.43 V and 0.50 V, respectively. Fig. 6c shows the OER LSV of FeN4-SAC, RuN4-DAC, and FeRuN6-DAC samples under O₂-saturated electrolyte. The OER onset potential and overpotential for the FeRuN6-DAC

sample are 1.50 V_{RHE} and 0.27 V, respectively. The experimental OER overpotential of 0.27 V is consistent with the DFT-predicted overpotential of 0.19 V. FeN4-SAC and RuN4-SAC display the OER onset potentials of 1.58 V_{RHE} and 1.62 V_{RHE} , leading to the OER overpotentials of 0.35 V and 0.39 V, respectively. Figs. 6b and d show the Tafel slope values obtained from the ORR and OER LSV curves. The FeRuN6-DAC sample possesses an ORR Tafel slope of 104 mVdec $^{-1}$, significantly lower than the ORR Tafel slopes of 386 mVdec $^{-1}$ for FeN4-SAC and 606 mVdec $^{-1}$ for RuN4-SAC. Besides, the FeRuN6-DAC sample

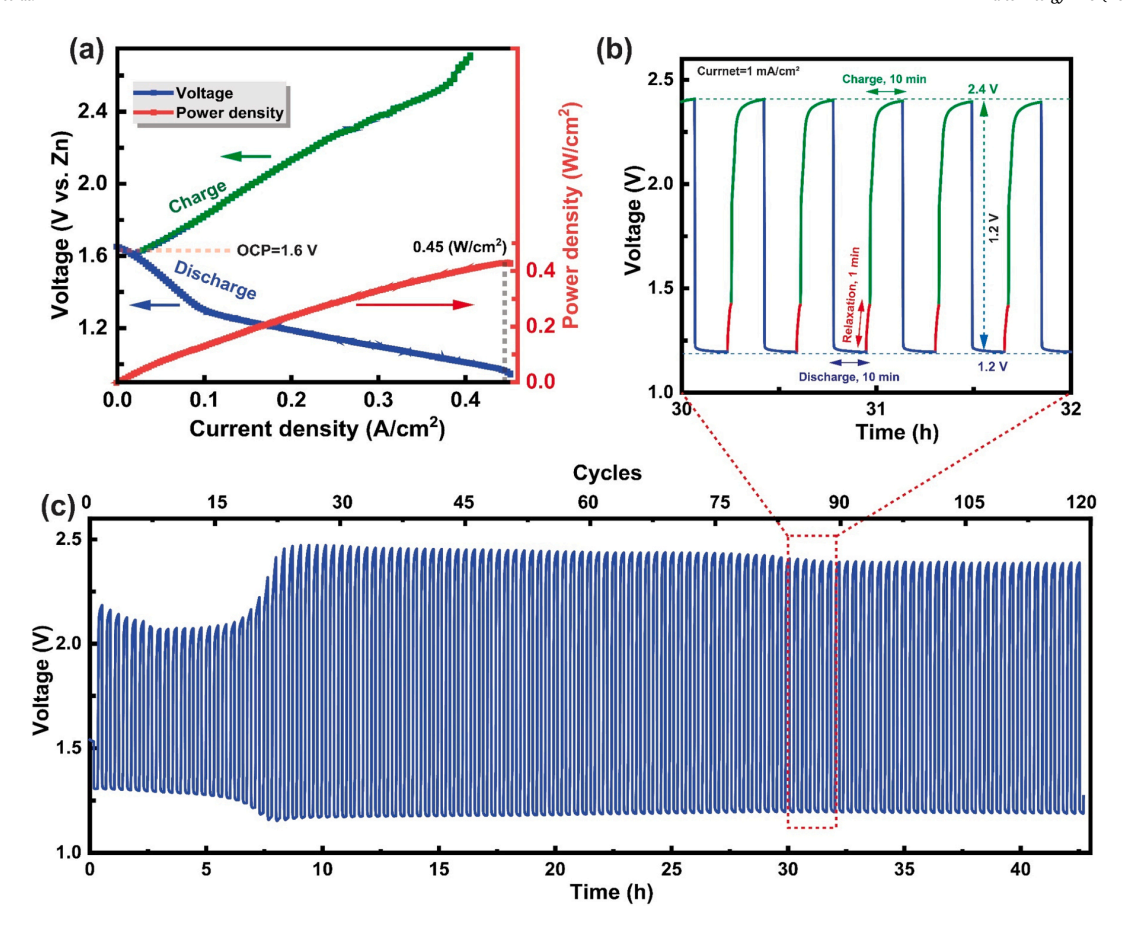


Fig. 7. Zinc-air battery performance. Polarization curve and power density plots of an assembled Zinc-air battery using FeRuN6-DAC in place of the cathode for discharge and charge processes. This indicates an open circuit potential (OCP) of around 1.6 V. (b,c) The galvanostatic discharge-charge curve at 1 mAcm⁻² under ambient air atmosphere for 40 hours and 120 cycles. 6 M KOH is used as the electrolyte for all results.

possesses an OER Tafel slope of $124~\rm mV dec^{-1}$, significantly lower than the OER Tafel slopes of $178~\rm mV dec^{-1}$ for FeN4-SAC and $201~\rm mV dec^{-1}$ for RuN4-SAC. The low ORR and OER Tafel slope values observed for FeRuN6-DAC indicate favorable ORR and OER kinetics.

In order to compare our theoretical and experimental results, we plot the experimental versus the DFT-obtained OER and ORR overpotentials at the current density of 1 mA/cm² for FeN4-SAC, RuN4-SAC, and FeRuN6-DAC. Fig. 6e, indicates good agreement between DFT and experimental results, with the best performance for FeRuN6-DAC. Therefore, our DFT calculations and experiments demonstrate that the combination of Fe and Ru metals in FeRuN6-DAC surpasses the ORR and OER activities of FeN4-SAC and RuN4-SAC due to their interactions in the DAC.

These good ORR and OER performances provide the opportunity for developing a rechargeable Zinc-air battery. Therefore, we tested the performance of the designed FeRuN6-DAC in a rechargeable Zinc-air battery setup. Fig. 7a shows discharge (blue line) and charge (green line) polarization curves and discharge power density (red line) plots of Zinc-air battery using FeRuN6-DAC in place of the cathode, leading to an open circuit potential (OCP) of 1.6 V versus Zinc. This indicates that the FeRuN6-DAC can give a maximum power density of 0.45 W/cm² at the current density of 0.44 A/cm². Fig. 7b,c show the galvanostatic discharge-charge plot of the Zinc-air battery with FeRuN6-DAC in place of cathodes for 40 hours at the current density of 1 mAcm², under ambient air atmosphere, using the 6 M KOH electrolyte. As provided in Fig. 7b, each charge and discharge process were set to 10 min in duration, following by 1 min duration for relaxation. The discharge and

charge potentials reach 1.2 V and 2.4 V, respectively, with a 1.2 V gap for the discharge and charge potentials. In addition, the stability of the catalyst for 120 discharge-charge cycles is confirmed in Fig. 7c. We found that the initial voltage for the Zinc-air battery is different for both the charge and discharge processes than the steady state long-time value, in agreement with the data reported in the literature [48,49]. We attribute these early-stage changes in the voltage to the fact that the zinc surface is quite clean without oxide on the surface and that there is no zinc ion in the electrolyte which can hugely affect the voltage of the zinc battery, especially in the charging process [49]. To show the durability of the prepared FeRuN6-DAC at high current densities, we performed the galvanostatic discharge of the Zinc-air battery for 13 hours at the current densities of 1 mAcm⁻² and 7.14 mAcm⁻² under ambient air atmosphere, using the 6 M KOH electrolyte (Figure S16). The current densities of 1 and 7.14 mAcm⁻² lead to the voltages of 1.28 and 0.98 V vs. Zn, and power densities of 110 and 632 mWh, respectively.

10. Conclusion

We performed the high-throughput computational screening for the rational design of dual atom catalysts (M_1M_2N6 -DAC) for the oxygen reduction and evolution reactions (ORR and OER), where M_1 and M_2 represent Fe, Co, Ni, Ru, Rh, Pd, Os, Ir, or Pt metals. Among all the combinations, FeRuN6-DAC shows the low predicted ORR and OER overpotentials of 0.24 V and 0.19 V, respectively, with Fe as the active site for both ORR and OER. The tuning of the Fe active site towards

facilitating the adsorption and desorption of OH* intermediate was confirmed based on *in-situ* electron spin resonance (ESR), indicating that the increase in the concentration of OH* intermediate on Fe, increases the spin state of Fe sites. Based on our hybrid density functional theory (DFT) calculations, we synthesized and characterized FeRuN6-DAC, FeN4-SAC, and RuN4-SAC samples. We observe that FeRuN6-DAC has an experimental ORR and OER overpotentials of 0.29 V and 0.24 V, respectively, with Tafel slopes of 104 mVdec⁻¹ and 124 mVdec⁻¹. The rechargeable Zinc-air battery setup was fabricated with FeRuN6-DAC in place of the cathode, showing good performance and stability after 120 cycles. Based on our theoretical and experimental findings, we designed a new catalyst for electrochemical ORR, OER, and Zinc-air battery applications.

CRediT authorship contribution statement

Shuguan Chen: Investigation. Zhengtang Luo: Writing – review & editing, Validation, Supervision, Methodology, Funding acquisition, Data curation, Conceptualization. Wenting Wu: Supervision, Data curation, Conceptualization. William A. Goddard III: Writing - review & editing, Validation, Supervision, Resources, Methodology, Investigation, Funding acquisition, Formal analysis, Data curation, Conceptualization. Mohsen Tamtaji: Writing - review & editing, Writing - original draft, Visualization, Validation, Methodology, Investigation, Formal analysis, Data curation, Conceptualization. GuanHua Chen: Writing – review & editing, Validation, Supervision, Resources, Methodology, Investigation, Funding acquisition, Formal analysis, Data curation, Conceptualization. Min Gyu Kim: Data curation. Zhimin Li: Data curation. Songhua Cai: Data curation. Jun WANG: Data curation. Patrick Ryan Galligan: Writing - review & editing, Visualization, Methodology, Data curation. Faan-Fung Hung: Data curation. Hui Guo: Methodology.

Declaration of Competing Interest

The authors declare the following financial interests/personal relationships which may be considered as potential competing interests: Guanhua chen has patent An Iron-Ruthenium Dual Atom Catalyst for Rechargeable Zinc-Air Battery pending to Guanhua Chen and Mohsen Tamtaji. If there are other authors, they declare that they have no known competing financial interests or personal relationships that could have appeared to influence the work reported in this paper.

Data availability

Data will be made available on request.

Acknowledgements

WAG thanks the US National Science Foundation (CBET-2311117) for support. GHC acknowledges financial supports by the General Research Fund (Grant No. 17309620) and Research Grants Council (RGC: T23-713/22-R). WAG and GHC acknowledge support from the Hong Kong Quantum AI Lab, AIR@InnoHK of the Hong Kong Government. Z.L. acknowledge supports by grants from the Research Grants Council of the Hong Kong Special Administrative Region, China (Project No. HKUST C6008-20E, 16304421), Research Fund of the Guangdong-Hong Kong-Macao Joint Laboratory for Intelligent Micro-Nano Opto-electronic Technology (2020B1212030010). The help from Chi Kin Jenkin Tsui is greatly appreciated on the Zinc-air battery setup fabrication and performance.

Associated content

Supporting Information (Word file)
Characterization, DFT calculations, Descriptor, and Machine

Learning on Gibbs free energies.

Appendix A. Supporting information

Supplementary data associated with this article can be found in the online version at doi:10.1016/j.nanoen.2024.109634.

References

- X. Li, Z. Xiang, Identifying the impact of the covalent-bonded carbon matrix to FeN4 sites for acidic oxygen reduction, Nat. Commun. 13 (2022), https://doi.org/ 10.1038/s41467.021.27735.1
- [2] Y. Wu, Q. Wu, Q. Zhang, Z. Lou, K. Liu, Y. Ma, Z. Wang, Z. Zheng, H. Cheng, Y. Liu, Y. Dai, B. Huang, P. Wang, An organometal halide perovskite supported Pt single-atom photocatalyst for H 2 evolution, Energy Environ. Sci. 15 (2022) 1271–1281, https://doi.org/10.1039/dlee03679c.
- [3] J. Wang, Z. Huang, W. Liu, C. Chang, H. Tang, Z. Li, W. Chen, C. Jia, T. Yao, S. Wei, Y. Wu, Y. Li, Design of N-Coordinated Dual-Metal Sites: a stable and active pt-free catalyst for acidic oxygen reduction reaction, J. Am. Chem. Soc. 139 (2017) 17281–17284, https://doi.org/10.1021/jacs.7b10385.
- [4] M. Feng, X. Wu, H. Cheng, Z. Fan, X. Li, F. Cui, S. Fan, Y. Dai, G. Lei, G. He, Well-defined Fe-Cu diatomic sites for efficient catalysis of CO2electroreduction, J. Mater. Chem. A. 9 (2021) 23817–23827, https://doi.org/10.1039/d1ta02833b.
- [5] Y. Li, B. Wei, M. Zhu, J. Chen, Q. Jiang, B. Yang, Y. Hou, L. Lei, Z. Li, R. Zhang, Y. Lu, Synergistic Effect of Atomically Dispersed Ni–Zn Pair Sites for Enhanced CO2 Electroreduction, Adv. Mater. 33 (2021) 2102212, https://doi.org/10.1002/ adma.202102212
- [6] T. He, B. Yu, Y. Zhang, X. Ouyang, S. Chen, Rational design of carbon-supported single and dual atom catalysts for bifunctional oxygen electrocatalysis, Curr. Opin. Electrochem. 37 (2022) 101197, https://doi.org/10.1016/j.coelec.2022.101197.
- [7] T. He, A.R.P. Santiago, Y. Kong, M.A. Ahsan, R. Luque, A. Du, H. Pan, Atomically Dispersed Heteronuclear Dual-Atom Catalysts: a new rising star in atomic catalysis, Small 18 (2021) 2106091, https://doi.org/10.1002/smll.202106091.
- [8] W. Li, J. Yang, D. Wang, Long-Range Interactions in Diatomic Catalysts Boosting Electrocatalysis, Angew. Chem. 134 (2022) e202213318, https://doi.org/10.1002/ ange.202213318.
- [9] Z. Zeng, L.Y. Gan, H. Bin Yang, X. Su, J. Gao, W. Liu, H. Matsumoto, J. Gong, J. Zhang, W. Cai, Z. Zhang, Y. Yan, B. Liu, P. Chen, Orbital coupling of heterodiatomic nickel-iron site for bifunctional electrocatalysis of CO2 reduction and oxygen evolution, Nat. Commun. 12 (1) (2021) 11, https://doi.org/10.1038/s41467.071.24052.5
- [10] N. Karmodak, S. Vijay, G. Kastlunger, K. Chan, Computational Screening of Single and Di-Atom Catalysts for Electrochemical CO 2 Reduction, ACS Catal. 12 (2022) 4818–4824, https://doi.org/10.1021/acscatal.1c05750.
- [11] Y. Cheng, S. He, J.P. Veder, R. De Marco, S. Ze Yang, S. Ping Jiang, Atomically Dispersed Bimetallic FeNi Catalysts as Highly Efficient Bifunctional Catalysts for Reversible Oxygen Evolution and Oxygen Reduction Reactions, ChemElectroChem 6 (2019) 3478–3487, https://doi.org/10.1002/celc.201900483.
- [12] Z. Xiao, P. Sun, Z. Qiao, K. Qiao, H. Xu, S. Wang, D. Cao, Atomically dispersed Fe-Cu dual-site catalysts synergistically boosting oxygen reduction for hydrogen fuel cells, Chem. Eng. J. 446 (2022) 137112, https://doi.org/10.1016/j.cei.2022.137112.
- [13] Y. Ma, H. Fan, C. Wu, M. Zhang, J. Yu, L. Song, K. Li, J. He, An efficient dual-metal single-atom catalyst for bifunctional catalysis in zinc-air batteries, Carbon N. Y 185 (2021) 526–535. https://doi.org/10.1016/j.carbon.2021.09.044.
- [14] Y. Wang, B.J. Park, V.K. Paidi, R. Huang, Y. Lee, K.J. Noh, K.S. Lee, J.W. Han, Precisely Constructing Orbital Coupling-Modulated Dual-Atom Fe Pair Sites for Synergistic CO2 Electroreduction, ACS Energy Lett. 7 (2022) 640–649, https://doi.org/10.1021/acsenergylett.1.002446
- org/10.1021/acsenergylett.1c02446.
 [15] L. Yu, F. Li, J. Zhao, Z. Chen, Revisiting catalytic performance of supported metal dimers for oxygen reduction reaction via magnetic coupling from first principles, Adv. Powder Mater. 1 (2022) 100031, https://doi.org/10.1016/j. apmate.2022.01.004.
- [16] F. Kong, R. Si, N. Chen, Q. Wang, J. Li, G. Yin, M. Gu, J. Wang, L.M. Liu, X. Sun, Origin of hetero-nuclear Au-Co dual atoms for efficient acidic oxygen reduction, Appl. Catal. B Environ. 301 (2022) 120782, https://doi.org/10.1016/j. appetth 2021 120782
- [17] F. Rehman, S. Kwon, C.B. Musgrave, M. Tamtaji, W.A. Goddard III, Z. Luo, High-throughput screening to predict highly active dual-atom catalysts for electrocatalytic reduction of nitrate to ammonia, Nano Energy. 103 (2022) 107866, https://doi.org/10.1016/j.nanoen.2022.107866.
- [18] G. Yang, J. Zhu, P. Yuan, Y. Hu, G. Qu, B.A. Lu, X. Xue, H. Yin, W. Cheng, J. Cheng, W. Xu, J. Li, J. Hu, S. Mu, J.N. Zhang, Regulating Fe-spin state by atomically dispersed Mn-N in Fe-N-C catalysts with high oxygen reduction activity, Nat. Commun. 12 (2021) 4–13, https://doi.org/10.1038/s41467-021-21919-5.
- [19] L. Jiao, J. Zhu, Y. Zhang, W. Yang, S. Zhou, A. Li, C. Xie, X. Zheng, W. Zhou, S. H. Yu, H.L. Jiang, Non-Bonding Interaction of Neighboring Fe and Ni Single-Atom Pairs on MOF-Derived N-Doped Carbon for Enhanced CO2Electroreduction, J. Am. Chem. Soc. 143 (2021) 19417–19424, https://doi.org/10.1021/jacs.1c08050.
- [20] J. Zhao, L. Zong, L. Cui, F. Lu, Z. Xiao, L. Wang, Synthesis of Dual-metal Single Atom in Porous Carbon Nanospheres with Enhanced Oxygen Reduction Activity in Both Acidic and Alkaline Electrolytes, J. Colloid Interface Sci. 633 (2022) 828–835, https://doi.org/10.1016/j.jcis.2022.11.147.

[21] M. Tong, F. Sun, Y. Xie, Y. Wang, Y. Yang, C. Tian, L. Wang, H. Fu, Operando Cooperated Catalytic Mechanism of Atomically Dispersed Cu–N4 and Zn–N4 for Promoting Oxygen Reduction Reaction, Angew. Chem. - Int. Ed. 60 (2021) 14005–14012, https://doi.org/10.1002/anie.202102053.

- [22] W.S. Hummers, R.E. Offeman, Preparation of Graphitic Oxide, J. Am. Chem. Soc. 80 (1958) 1339, https://doi.org/10.1021/ja01539a017.
- [23] M.D. Hossain, Z. Liu, M. Zhuang, X. Yan, G.L. Xu, C.A. Gadre, A. Tyagi, I.H. Abidi, C.J. Sun, H. Wong, A. Guda, Y. Hao, X. Pan, K. Amine, Z. Luo, Rational Design of Graphene-Supported Single Atom Catalysts for Hydrogen Evolution Reaction, Adv. Energy Mater. 9 (2019) 1803689, https://doi.org/10.1002/aenm.201803689.
- [24] K. Khan, T. Liu, M. Arif, X. Yan, M.D. Hossain, F. Rehman, S. Zhou, J. Yang, C. Sun, S.H. Bae, J. Kim, K. Amine, X. Pan, Z. Luo, Laser-Irradiated Holey Graphene-Supported Single-Atom Catalyst towards Hydrogen Evolution and Oxygen Reduction, Adv. Energy Mater. 11 (2021) 2101619, https://doi.org/10.1002/aepm.202101619.
- [25] X. Hai, S. Xi, S. Mitchell, K. Harrath, H. Xu, D.F. Akl, D. Kong, J. Li, Z. Li, T. Sun, H. Yang, Y. Cui, C. Su, X. Zhao, J. Li, J. Pérez-ramírez, J. Lu, Scalable two-step annealing method for preparing ultra-high-density single-atom catalyst libraries, Nature Nanotechnology 17 (2022) 174–181, https://doi.org/10.1038/s41565-021-01022-y.
- [26] M.J. Hülsey, B. Zhang, Z. Ma, H. Asakura, D.A. Do, W. Chen, T. Tanaka, P. Zhang, Z. Wu, N. Yan, In situ spectroscopy-guided engineering of rhodium single-atom catalysts for CO oxidation, Nat. Commun. 10 (2019) 1330, https://doi.org/10.1038/s41467-019-09188-9
- [27] G. Xu, C. Li, C. Chi, L. Wu, Y. Sun, J. Zhao, X.-H. Xia, S. Gou, A supramolecular photosensitizer derived from an Arene-Ru(II) complex self-assembly for NIR activated photodynamic and photothermal therapy, Nat. Commun. 13 (2022) 3064. https://doi.org/10.1038/s41467-022-30721-w.
- [28] M. Tamtaji, S. Cai, W. Wu, T. Liu, Z. Li, H.Y. Chang, P.R. Galligan, S.I. Iida, X. Li, F. Rehman, K. Amine, W.A. Goddard III, Z. Luo, Single and dual metal atom catalysts for enhanced singlet oxygen generation and oxygen reduction reaction, J. Mater. Chem. A. 11 (2023) 7513–7525, https://doi.org/10.1039/d2ta08240c.
- [29] A.V. Marenich, C.J. Cramer, D.G. Truhlar, Universal solvation model based on solute electron density and on a continuum model of the solvent defined by the bulk dielectric constant and atomic surface tensions, J. Phys. Chem. B. 113 (2009) 6378–6396, https://doi.org/10.1021/jp810292n.
- [30] T. Lu, F. Chen, Multiwfn: A multifunctional wavefunction analyzer, J. Comput. Chem. 33 (2012) 580–592. https://doi.org/10.1002/jcc.22885.
- Chem. 33 (2012) 580–592, https://doi.org/10.1002/jcc.22885.
 [31] M. Tamtaji, X. Guo, A. Tyagi, P.R. Galligan, Z. Liu, A. Roxas, H. Liu, Y. Cai, H. Wong, L. Zeng, J. Xie, Y. Du, Z. Hu, D. Lu, W.A. Goddard III, Y. Zhu, Z. Luo, Machine Learning-Aided Design of Gold Core-Shell Nanocatalysts toward Enhanced and Selective Photooxygenation, ACS Appl. Mater. Interfaces 14 (2022) 46471–46480, https://doi.org/10.1021/acsami.2c11101.
- [32] M. Tamtaji, H. Gao, M.D. Hossain, P.R. Galligan, H. Wong, Z. Liu, H. Liu, Y. Cai, W. A. Goddard III, Z. Luo, Machine learning for design principles for single atom catalysts towards electrochemical reactions, J. Mater. Chem. A. 10 (2022) 15309–151331, https://doi.org/10.1039/d2ta02039d.
- [33] M. Tamtaji, C. Chen, Z. Hu, W.A. Goddard III, G. Chen, A Surrogate Machine Learning Model for the Design of Single-Atom Catalyst on Carbon and Porphyrin Supports towards Electrochemistry, The Journal of Physical Chemistry C 12 (2023) 9992–10000, https://doi.org/10.1021/acs.jpcc.3c00765.
- [34] X. Mi, B. Zou, F. Zou, J. Hu, Permutation-based identification of important biomarkers for complex diseases via machine learning models, Nat. Commun. 12 (2021) 3008, https://doi.org/10.1038/s41467-021-22756-2.
- [35] G. Panapitiya, G. Avendano-Franco, P. Ren, X. Wen, Y. Li, J.P. Lewis, Machine-Learning Prediction of CO Adsorption in Thiolated, Ag-Alloyed Au Nanoclusters,

- J. Am. Chem. Soc. 140 (2018) 17508–17514, https://doi.org/10.1021/iacs.8b08800.
- [36] X. Li, C.S. Cao, S.F. Hung, Y.R. Lu, W. Cai, A.I. Rykov, S. Miao, S. Xi, H. Yang, Z. Hu, J. Wang, J. Zhao, E.E. Alp, W. Xu, T.S. Chan, H. Chen, Q. Xiong, H. Xiao, Y. Huang, J. Li, T. Zhang, B. Liu, Identification of the Electronic and Structural Dynamics of Catalytic Centers in Single-Fe-Atom Material, Chem 6 (2020) 3440–3454, https://doi.org/10.1016/j.chempr.2020.11.027.
- [37] H. Xu, D. Cheng, D. Cao, X.C. Zeng, A universal principle for a rational design of single-atom electrocatalysts, Nat. Catal. 1 (2018) 339–348, https://doi.org/ 10.1038/ed1920.018.00632.
- [38] K. Khan, X. Yan, Q. Yu, S.H. Bae, J.J. White, J. Liu, T. Liu, C. Sun, J. Kim, H. M. Cheng, Y. Wang, B. Liu, K. Amine, X. Pan, Z. Luo, Stone-Wales defect-rich carbon-supported dual-metal single atom sites for Zn-air batteries, Nano Energy 90 (2021) 106488. https://doi.org/10.1016/j.nanoen.2021.106488.
- [39] A. Kulkarni, S. Siahrostami, A. Patel, J.K. Nørskov, Understanding Catalytic Activity Trends in the Oxygen Reduction Reaction, Chem. Rev. 118 (2018) 2302–2312, https://doi.org/10.1021/acs.chemrev.7b00488.
- [40] M. Tamtaji, Q. Peng, T. Liu, X. Zhao, Z. Xu, P.R. Galligan, M.D. Hossain, Z. Liu, H. Wong, H. Liu, K. Amine, Y. Zhu, W.A. Goddard III, W. Wu, Z. Luo, Non-bonding interaction of dual atom catalysts for enhanced oxygen reduction reaction, Nano Energy 108 (2023) 108218, https://doi.org/10.1016/j.nanoen.2023.108218.
- [41] J. Zhang, A. Yu, C. Sun, Computational exploration of dual atom catalysts loaded on defective graphene for oxygen reduction reaction, Appl. Surf. Sci. 605 (2022) 154534 https://doi.org/10.1016/j.apsusc.2022.154534
- [42] T. Liu, Y. Wang, Y. Li, How pH Affects the Oxygen Reduction Reactivity of Fe-N-C Materials, ACS Catal. 13 (2023) 1717–1725, https://doi.org/10.1021/ acsental 2c05540
- [43] H.Bin Yang, S.F. Hung, S. Liu, K. Yuan, S. Miao, L. Zhang, X. Huang, H.Y. Wang, W. Cai, R. Chen, J. Gao, X. Yang, W. Chen, Y. Huang, H.M. Chen, C.M. Li, T. Zhang, B. Liu, Atomically dispersed Ni(i) as the active site for electrochemical CO2 reduction, Nat. Energy 3 (2018) 140–147, https://doi.org/10.1038/s41560-017-0078-8
- [44] L. Jiao, J. Zhu, Y. Zhang, W. Yang, S. Zhou, A. Li, C. Xie, X. Zheng, W. Zhou, S. Yu, H. Jiang, Non-Bonding Interaction of Neighboring Fe and Ni Single-Atom Pairs on MOF-Derived N - Doped Carbon for Enhanced CO2 Electroreduction, JACS 143 (2021) 19417–19424, https://doi.org/10.1021/jacs.1c08050.
- [45] O. Bunău, Y. Joly, Self-consistent aspects of x-ray absorption calculations, J. Phys. Condens. Matter 21 (2009) 345501, https://doi.org/10.1088/0953-8984/21/34/ 345501
- [46] A. Nandy, D.B.K. Chu, D.R. Harper, C. Duan, N. Arunachalam, Y. Cytter, H.J. Kulik, Large-scale comparison of 3d and 4d transition metal complexes illuminates the reduced effect of exchange on second-row spin-state energetics, Phys. Chem. Chem. Phys. 22 (2020) 19326–19341, https://doi.org/10.1039/d0cp02977g.
- [47] A. Eckmann, A. Felten, I. Verzhbitskiy, R. Davey, C. Casiraghi, Raman study on defective graphene: effect of the excitation energy, type, and amount of defects, Phys. Rev. B - Condens. Matter Mater. Phys 88 (2013) 035426, https://doi.org/ 10.1103/PhysRevB.88.035426.
- [48] H. Sun, S. Liu, M. Wang, T. Qian, J. Xiong, C. Yan, Updating the Intrinsic Activity of a Single-Atom Site with a P-O Bond for a Rechargeable Zn-Air Battery, ACS Appl. Mater. Interfaces 11 (2019) 33054–33061, https://doi.org/10.1021/ acsami.9h11337
- [49] Y. Li, C.B. Musgrave, M.Y. Yang, M.M. Kim, K. Zhang, M. Tamtaji, Y. Cai, T. W. Tang, J. Wang, B. Yuan, W.A. Goddard III, Z. Luo, The Zn deposition mechanism and pressure effects for aqueous Zn batteries: a combined theoretical and experimental study, Adv. Energy Mater. 14 (2024) 2303047, https://doi.org/10.1002/aenm.202303047.